Scale-Adaptive Simulation of Transient Two-Phase Flow in Continuous-Casting Mold

ZHONGQIU LIU, ALEXANDER VAKHRUSHEV, MENGHUAI WU, ABDELLAH KHARICHA, ANDREAS LUDWIG, and BAOKUAN LI

Scale-adaptive simulation (SAS) of the transient gas–liquid two-phase flow in a laboratory-scale continuous-casting mold is presented. The main objective is to investigate the applicability of the scale-adaptive unsteady Reynolds-averaged Navier–Stokes turbulent model (URANS SAS) for predicting the transient multiscale turbulent structures in a two-phase flow. Good quantitative agreements with the experimental data and the large eddy simulation (LES) results are obtained both for the time-averaged velocity field and for the transient turbulent characteristics. The introduction of the von Karman length-scale into the turbulence-scale equation allows the SAS model to dynamically adjust to the resolved turbulent structures. The LES-like pulsating behavior of the air gas and the large-scale liquid eddy magnitudes in the unsteady regions of flow field are captured by the SAS model. The classical − 5/3 law of power spectrum density (PSD) of the axial velocity is kept properly for the single-phase turbulent flow. For two-phase flow, the decay of PSD is too steep at the high-frequency region; the predicted PSD obtained with SAS is damped stronger than that estimated by LES. The SAS model offers an attractive alternative to the existing LES approach or to the other hybrid RANS/LES models for strongly unsteady flows.

https://doi.org/10.1007/s11663-018-1443-0

I. INTRODUCTION

DURING the continuous-casting (CC) process of aluminum-killed steel, argon gas is usually injected into the submerged entry nozzle (SEN) to prevent nozzle clogging due to nonmetallic inclusions (Al_2O_3 particles) attaching to the inner wall of the SEN. The injected gas is usually in the form of bubbles, being transported by the steel melt into the mold. The nature of the flow is multiphase turbulence. Understanding the gas–liquid multiphase turbulent flow is important to control the transport of nonmetallic inclusions, the fluctuation of slag–steel interface (one cause of slag entrapment), and other undesired effects.[1–3]

The multiphase turbulent flow in the CC mold can be characterized by eddies with a wide range of spatial and temporal scales. The spatial scales of turbulent eddy are bounded by the integral scale of flow field and the diffusive action of molecular viscosity. The largest scales are typically comparable to the characteristic length of the mean flow and depend on the mold geometry and casting conditions. The smaller scales depend on the bubble dynamics and are proportional to the bubble size. The smallest scale relates to the Kolmogorov scale[4] and is generally smaller than the bubble size. Consistently, the turbulence kinetic energy of the flow will be dissipated into heat by the smallest scale eddies.

The computational fluid dynamics (CFD) has been widely used in designing and optimizing the CC process for the past several decades. Reliable turbulence modeling is required to obtain the accurate flow pattern prediction. Three approaches are typically distinguished for the turbulent-flow modeling: direct numerical simulation (DNS), Reynolds-averaged Navier–Stokes (RANS), and large eddy simulation (LES). According to the DNS approach, the whole range of spatial and temporal scales of turbulence can be resolved on the computational grid, from the smallest dissipative scale up to the integral scale, associated with the motions containing most of the kinetic energy.[5] The computational cost of DNS is extremely high, and it increases with the cube of the Reynolds number,[6] so that DNS is inapplicable to the high

ZHONGQIU LIU is with the School of Metallurgy, Northeastern University, No. 3-11, Wenhua Road, Heping District, Shenyang 110819, China and also with the Christian Doppler Laboratory for Advanced Process Simulation of Solidification and Melting, Montanuniversität Leoben, Leoben, Austria. Contact e-mail: liuzq@smm.neu.edu.cn ALEXANDER VAKHRUSHEV, MENGHUAI WU, and ABDELLAH KHARICHA are with the Christian Doppler Laboratory for Advanced Process Simulation of Solidification and Melting, Montanuniversität Leoben. ANDREAS LUDWIG is with the Chair of Simulation and Modeling of Metallurgical Processes Department of Metallurgy, Montanuniversität Leoben. BAOKUAN LI is with the School of Metallurgy, Northeastern University.

Manuscript submitted June 20, 2018.
Article published online October 30, 2018.

Reynolds number flows. The RANS models, *e.g.*, k–ε, k–ω, shear stress transport (SST) and Reynolds stress model (RSM), provide the mean flow results with engineering accuracy at moderate computational cost. However, limited by their isotropic nature and due to the eddy-viscosity hypothesis, even at the unsteady mode (URANS), they struggle to predict the details of flow separation or anisotropic turbulence. In LES, the turbulence flow is filtered to obtain large- and small-scale eddies. Large eddies are resolved directly, while small ones are modeled with the subgrid scale (SGS) model. Currently, LES has been identified as a better way to model the turbulence in the CC process.[7–11] However, it still require rather fine grids, especially at the boundary layers. Recently, the scale-adaptive simulation (SAS) approach based on an improved length-scale equation for turbulence modeling has been proposed by Menter and Egorov.[12–14] It is an improved URANS model allowing the formation of a turbulent spectrum by adjusting its length-scale to the resolved structures. It can offer many interesting characteristics like other hybrid RANS–LES combinations and generally requires less computational effort.

Simulations of the two-phase flow in the CC process have been performed by different researchers combining the Euler–Euler model with the (U) RANS or LES turbulence models. The (U) RANS method has been widely used, especially the k–ε model family. Thomas *et al.*[15] simulated the steady-state argon gas / molten steel two-phase flow based on the standard k–ε model. The influence of the argon gas injection on the melt flow was investigated, whereas the bubble-induced turbulence (BIT) was ignored. Creech[16] quantified how the detrimental transition from the double- to single-roll pattern could be avoided in the mold by keeping the gas rate below a critical value. Bai *et al.*[17] simulated a time-averaged two-phase turbulent flow in a slide-gate tundish nozzle, considering an empirical interphase drag force between molten steel and argon bubbles. Ramos-Banderas *et al.*[18] studied the dynamics of a two-phase downward flow in the SEN and its influence on the two-phase flow in the mold using a modified k–ε model. Klostermann *et al.*[19] studied the gas–liquid flow in a stopper rod-controlled SEN using a modified k–ε model as well, considering the Tcheu's theory[20] for the turbulent distribution of the gas bubbles. Liu *et al.*[21] developed an Euler–Euler–Lagrangian approach to study the influence of the argon gas injection on the molten steel flow and on the particle transport behavior in the mold. The modified k–ε model with extra source term to account for the BIT is adopted. Recently, the Euler–Euler approach combined with RANS turbulent models has been extended to enable the spatial variations in bubble size, and size evolution according to a population balance framework *via* the MUlti-SIze Group (MUSIG) model[22–24] and Average Bubble Number Density (ABND) model.[25] Timmel *et al.*[26] used the SST turbulent model to simulate the liquid–metal two-phase flow according to the frequently referenced experiment at the LIMMCAST facility at Helmholtz–Zentrum Dresden–Rossendrf (HZDR), considering the effect of electromagnetic brake or stirring. Sarkar *et al.*[27] studied the time-averaged meniscus flow and turbulence intensity distribution in the mold under the influences of argon injection and a double-ruler magnetic field. Euler–Euler Large eddy simulation (EELES) model has been developed by Liu *et al.*[28] to capture the transient asymmetrical two-phase flow in the mold. Then they used the EELES with the dynamic SGS model to simulate the transient gas–liquid flow.[29] The EELES model can capture more details of the two-phase turbulent-flow characteristics, including multiscale vortex structures, vorticity distribution, etc. Furthermore, a detailed review on modeling and simulation of CC process can be found in the recent study from Thomas.[30] SAS has been successfully used to simulate the hot buoyant jet in the cross flow in a channel,[14] turbulent combustion in a swirl burner,[14] aerodynamic flows with massive separation,[31] and the dispersed bubbly flow in a bubble column.[32] All the results indicated that the SAS model leads to an improved result compared to (U) RANS simulations. However, relatively little study has been reported on the SAS modeling of turbulent flow in the CC mold.[33]

The current study attempts to perform a sensitivity analysis of the SAS for modeling the transient two-phase flow in a CC mold. To the best of the author's knowledge, the SAS is for the first time applied in this study for the transient two-phase flow in the mold. Both the experimental data measured by a laser Doppler velocimetry reported by Iguchi and Kasai[1] and previous investigations using LES modeling[29] were used to validate the current SAS model.

II. MATHEMATICAL MODEL

A. *Euler–Euler Two-Fluid Model*

In the Euler–Euler two-fluid model, conservation equations of mass and momentum for each phase m are given as follows:

$$\frac{\partial(\alpha_m \rho_m)}{\partial t} + \nabla \cdot (\alpha_m \rho_m \mathbf{u}_m) = 0 \qquad [1]$$

$$\frac{\partial(\alpha_m \rho_m \mathbf{u}_m)}{\partial t} + \nabla \cdot (\alpha_m \rho_m \mathbf{u}_m \mathbf{u}_m) = -\nabla \cdot (\alpha_m \boldsymbol{\tau}_m) - \alpha_m \nabla P + \alpha_m \rho_m \mathbf{g} + \mathbf{F}_m, \qquad [2]$$

where the lower index m denotes the phases. α, ρ, t, and $\mathbf{u}$ are the volume fraction, density, time, and velocity, respectively. All the phases share a single pressure field P. The terms on the right-hand side of Eq. [2], respectively, represent the stress, the pressure gradient, gravity, and interfacial forces.

The stress term of m phase is described as follows:

$$\tau_m = -\mu_{\text{eff},m}\left[\nabla \mathbf{u}_m + (\nabla \mathbf{u}_m)^T - \frac{2}{3}\mathbf{I}(\nabla \cdot \mathbf{u}_m)\right]. \qquad [3]$$

The effective viscosity of the liquid phase, $\mu_{\text{eff,l}}$, is composed of three contributions: the molecular viscosity, μ_{l}; the turbulent viscosity, $\mu_{\text{T,l}}$; and an extra term due to bubble-induced turbulence (BIT), $\mu_{\text{BI,l}}$. I is the unit tensor.

$$\mu_{\text{eff,l}} = \mu_{\text{l}} + \mu_{\text{T,l}} + \mu_{\text{BI,l}} \quad [4]$$

The effective viscosity of the gas phase is based on the effective liquid viscosity as was proposed by Jakobsen *et al.*[34]

$$\mu_{\text{eff,g}} = \frac{\rho_{\text{g}}}{\rho_{\text{l}}}\mu_{\text{eff,l}}, \quad [5]$$

where the subscript l denotes the liquid phase, and g denotes the gas phase.

In bubbly flows, the smallest scales are responsible for the dissipation of the turbulent kinetic energy as in the single-phase flow. However, the bubbles can also generate backscatter, *i.e.*, energy transfer from smaller to larger scales as reported by Dhotre *et al.*[35] The combination of both effects can yield an overall enhancement or an attenuation of the turbulence intensity. The model proposed by Sato *et al.*[36] has been used to take into account of the turbulence induced by the movement of the bubbles. The defining expression is

$$\mu_{\text{BI,l}} = \rho_{\text{l}} C_{\mu,\text{BI}} \alpha_{\text{g}} d_{\text{b}} \left|\mathbf{u}_{\text{g}} - \mathbf{u}_{\text{l}}\right| \quad [6]$$

with a model constant $C_{\mu,\text{BI}}$ equal to 0.6. The bubble diameter d_{b} is accepted to be a constant in this study.

B. *Turbulence Models*

In the current study, the turbulence is treated differently for different phases. Considering the low density and the flow rate of gas phase, the turbulence of dispersed gas bubble is calculated with a simple zero equation model. For the continuous liquid phase, both the unsteady SAS model and LES are used.

1. *Scale-adaptive simulation*

The SAS concept is based on the introduction of the von Karman length-scale (L_{vk}) into the turbulence-scale equation. Additionally acquired information allows the SAS model to dynamically adjust itself resolving the LES-like structures in the unsteady regions of the flow field. Recently, Menter and Egorov[12] proposed that the L_{vk} term can be transformed and implemented into any scale-defining equation, *e.g.*, employing the SST two-equation system to form the SST–SAS turbulence model. The governing equations of the SST–SAS model differ from those of the SST–RANS model[37] through introducing an additional scale-adaptive source term Q_{SAS} in the transport equation for the specific turbulence dissipation ω (also referred as turbulence eddy frequency). The equations for the turbulent kinetic energy k and the specific turbulence dissipation ω can be defined as

$$\frac{\partial(\rho_{\text{l}}\alpha_{\text{l}}k)}{\partial t} + \nabla\cdot(\alpha_{\text{l}}\rho_{\text{l}}\mathbf{u}_{\text{l}}k) = \alpha_{\text{l}}P_{\text{k}} - \alpha_{\text{l}}\rho c_{\mu}k\omega + \nabla\cdot\left(\alpha_{\text{l}}\left(\mu_{\text{l}} + \frac{\mu_{\text{T,l}}}{\sigma_k}\right)\nabla k\right) \quad [7]$$

$$\begin{aligned}\frac{\partial(\rho_{\text{l}}\alpha_{\text{l}}\omega)}{\partial t} + \nabla\cdot(\alpha_{\text{l}}\rho_{\text{l}}\mathbf{u}_{\text{l}}\omega) &= \alpha_{\text{l}}\frac{\omega}{k}P_k\left[1 - \zeta_1 + \zeta_2\left(\frac{L}{L_{vk}}\right)^2\right] \\ &-\alpha_{\text{l}}\rho_{\text{l}}\omega^2\left(c_{\mu} - c_{\mu}^{1/4}\zeta_3\right) + \alpha_{\text{l}}Q_{\text{SAS}} + \nabla\cdot\left(\alpha_l\frac{\mu_{T,l}}{\sigma_{\Phi}}\nabla\omega\right) \\ &+\alpha_l\frac{2\rho_l}{\sigma_{\Phi}}\left(\frac{1}{\omega}\nabla k\cdot\nabla\omega - \frac{k}{\omega^2}\nabla\omega\cdot\nabla\omega\right),\end{aligned} \quad [8]$$

where P_k is the turbulent production term depending on the rate of strain tensor $\mathbf{S}$ as follows:

$$P_k = \mu_{\text{T,l}}\mathbf{S}^2, \quad \text{with} \quad |\mathbf{S}| = \sqrt{2S_{ij}S_{ij}}, \quad S_{ij} = \frac{1}{2}\left(\frac{\partial u_{l,i}}{\partial x_j} + \frac{\partial u_{l,j}}{\partial x_i}\right), \quad [9]$$

where L is the length-scale of the modeled turbulence,

$$L = \sqrt{k}/(c_{\mu}^{1/4}\cdot\omega), \quad [10]$$

where L_{vk} is the von Karman length-scale.

$$L_{\text{vk}} = \max\left[\frac{\kappa\mathbf{S}}{|\mathbf{u}'_{\text{l}}|}, C_{S1}C_{SAS}\Delta\right], \quad \text{with} \quad |\mathbf{u}'_l| = \sqrt{\sum_{(i)}\left(\frac{\partial^2\mathbf{u}_{l,i}}{\partial x_j\partial x_j}\right)^2}. \quad [11]$$

The additional source term Q_{SAS} is defined by

$$Q_{\text{SAS}} = \max\left\{\rho\zeta_2\kappa\mathbf{S}^2\left(\frac{L}{L_{vk}}\right)^2 - C_{S1}\cdot\frac{2\rho_l k}{\sigma_{\Phi}}\cdot\max\left[\frac{1}{\omega^2}\nabla\omega\nabla\omega; \frac{1}{k^2}\nabla k\nabla k\right]; 0\right\}. \quad [12]$$

The values of the constants in above equations are $\zeta_1 = 0.8$, $\zeta_2 = 3.51$, $\zeta_3 = 0.0288$, $\sigma_{\Phi} = 2/3$, $\kappa = 0.41$, $c_{\mu} = 0.09$, and $C_{\text{S1}} = 2$. The SGS filter width Δ is equal to the cubic root of the control volume.

The equilibrium eddy viscosity of the SAS model can be defined by

$$\mu_{\text{T,l}} = \rho_{\text{l}}\left(\frac{1}{C_{\text{SAS}}}\cdot L_{vk}\right)^2|\mathbf{S}|, \quad [13]$$

where the model constant C_{SAS} is chosen to be 0.131. This formula has a similar structure as one for the Smagorinsky eddy viscosity used for the LES described in the next section.

2. *Large eddy simulation*

In the LES model, the key element is the SGS model which determines the effect of the unresolved turbulent scales. The model proposed by Smagorinsky[38] is used to calculate the turbulent viscosity $\mu_{T,l}$.

$$\mu_{T,l} = \rho_l (C_S \Delta)^2 \left|\bar{\mathbf{S}}\right|, \quad [14]$$

where the superscript "–" denotes the first filtering; C_S is the Smagorinsky constant. It was found that the best results for a wide range of flows are obtained for $C_S \approx 0.1$. However, employing a constant parameter is the most critical shortcoming of this simplified model.

In view of the uncertainty in specifying the constant C_S, Germano *et al.*[39] proposed a dynamic SGS model. Then, Lilly[40] proposed a modification of Germano's model, in which the C_S is not arbitrarily chosen, but is computed by

$$C_S = \sqrt{\frac{L_{ij} M_{ij}}{2 M_{ij}^2}} \quad [15]$$

$$L_{ij} = -\widehat{u_i u_j} + \hat{\bar{u}}_i \hat{\bar{u}}_j \quad [16]$$

$$M_{ij} = \hat{\Delta}^2 \left|\hat{\bar{S}}\right| \hat{\bar{S}}_{ij} - \Delta^2 \widehat{\left|\bar{S}\right| \bar{S}_{ij}}, \quad [17]$$

where the L_{ij} and M_{ij} are the assumed Gaussian variables. The concept of the dynamic procedure is to apply a second filter (called the test filter) to the equations of motion. The superscript "^" denotes the secondary filtering. The new filter width $\hat{\Delta}$ is twice the width of the initial grid filter Δ. Both filters produce a resolved flow field. The difference between them reflects the contribution of the small scales being in-between the filter sizes. The details of this filtering procedure can be seen elsewhere.[39,40]

C. *Interfacial Forces*

In the Euler–Euler model, the interfacial momentum transfer exhibits a dominant effect in the multiphase momentum equations. There is still no agreement in the community on the universal closures to be used. In the current study, the drag force F_D, lift force F_L, virtual mass force F_{VM}, and turbulent dispersion force F_{TD} are considered.

$$\mathbf{F}_m = \mathbf{F}_{lg} = -\mathbf{F}_{gl} = \mathbf{F}_D + \mathbf{F}_L + \mathbf{F}_{VM} + \mathbf{F}_{TD}, \quad [18]$$

where $\mathbf{F}_{lg}$ denotes the momentum transfer terms from the gas phase to liquid and vice versa for $\mathbf{F}_{gl}$.

$$\mathbf{F}_D = -\frac{3}{4} \alpha_g \rho_l \frac{C_D}{d_b} \left|\mathbf{u}_g - \mathbf{u}_l\right| (\mathbf{u}_g - \mathbf{u}_l) \quad [19]$$

$$\mathbf{F}_L = \alpha_g \rho_l C_L (\mathbf{u}_g - \mathbf{u}_l) \times \nabla \times \mathbf{u}_l \quad [20]$$

$$\mathbf{F}_{VM} = \alpha_g \rho_l C_{VM} \left(\frac{D\mathbf{u}_g}{Dt} - \frac{D\mathbf{u}_l}{Dt} \right) \quad [21]$$

$$\mathbf{F}_{TD} = C_{TD} C_D \frac{\nu_{t,g}}{\sigma_{t,g}} \left(\frac{\nabla \alpha_l}{\alpha_l} - \frac{\nabla \alpha_g}{\alpha_g} \right), \quad [22]$$

where C_D is the drag force coefficient, which can be evaluated by correlation of several distinct Reynolds number ranges for the individual bubbles as proposed by Ishii and Zuber.[41] The lift force coefficient C_L is set to 0.5 based on the study of Drew and Lahey.[42] The virtual mass force coefficient C_{VM} is taken to be 0.5 for spherical bubbles. According to standard model values, the turbulent dispersion coefficient of the gas phase $C_{TD,g} = 1$ and the turbulence Schmidt number of the gas phase $\sigma_{t,g} = 0.9$ are adopted here. The turbulence dispersion force is not employed within the LES due to the high turbulent structure resolution, which allows naturally for track dispersion mechanisms of the gas phase in the liquid flow.

III. EXPERIMENTAL DATA AND SIMULATION SETUP

A. *Experimental Data*

The experimental trials were carried out for the horizontal air–water flow in a well-designed apparatus, schematically shown in Figure 1.[1] The mold has a rectangular cross section of 0.3 m×0.15 m filled with water up to a height of 0.4 m. The mixed water and air are supplied into the mold through a nozzle with a diameter of 9 mm. Water circulates in the circuit through a buffer tank to the mold. The water flow rate and air flow rate are controlled by corresponding flow meters. In order to control the level of the free surface,

an overflow pipe is mounted at the right side of the mold. Measurements are performed along the mold's centerline at the nozzle inlet level (red line in Figure 1) for the water flow rate of 5 l/min. Once the water and air flows reach a quasi-steady-state regime, the water–air two-phase flow is captured using a video camera. The horizontal and vertical velocity components of the liquid phase are simultaneously measured by a two-channel laser Doppler velocimetry. Air bubbles are detected in the size range of 0.3 to 5 mm. More experimental details can be found in the study of Iguchi and Kasai.[1]

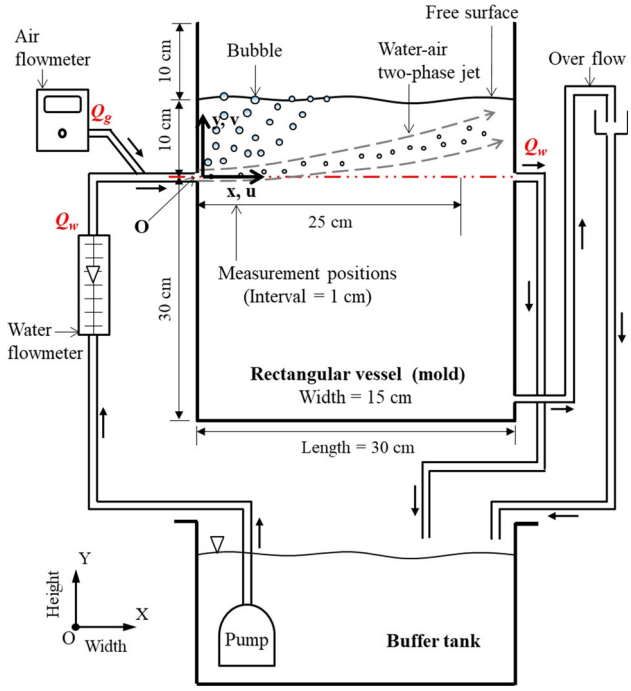

Fig. 1—Schematic of Iguchi's experimental apparatus, reprinted from Ref. [1] (Color figure online).

B. *Simulation Setup*

Numerical simulations are performed employing the CFD code ANSYS-CFX-14.5 combined with the CFX command language (CCL). The calculation domain (geometry), material properties, and boundary conditions were set corresponding to the water model as reported in Iguchi *et al.*[1] A mass flow rate boundary condition was used at the inlet, and the volume ratio of gas was estimated based on the water experiment. The bubbles are treated as monodispersed with a constant diameter of 3 mm, which corresponds to experiment observations. The top surface of the mold cavity is modeled as a degassing boundary condition, which means an outlet for the dispersed gas phase. Along the walls, a no-slip boundary condition is applied for the continuous phase and a free slip condition for the dispersed gas bubbles. At the outlet, a water mass flow is fixed assuming that no gas can go with the outflow.

A second-order, center-differencing scheme was used for the spatial discretization; while a first-order, fully implicit, backward-differencing scheme was employed for the time discretization. The SIMPLEC algorithm was employed for the pressure–velocity coupling. The time step of all simulations is 0.001 second. The choice of the time step is determined by the criterion that the maximum Courant–Friedrichs–Levy (CFL) number must be less than one (*i.e.*, $\Delta t \leqslant \Delta/|u|$). Converged

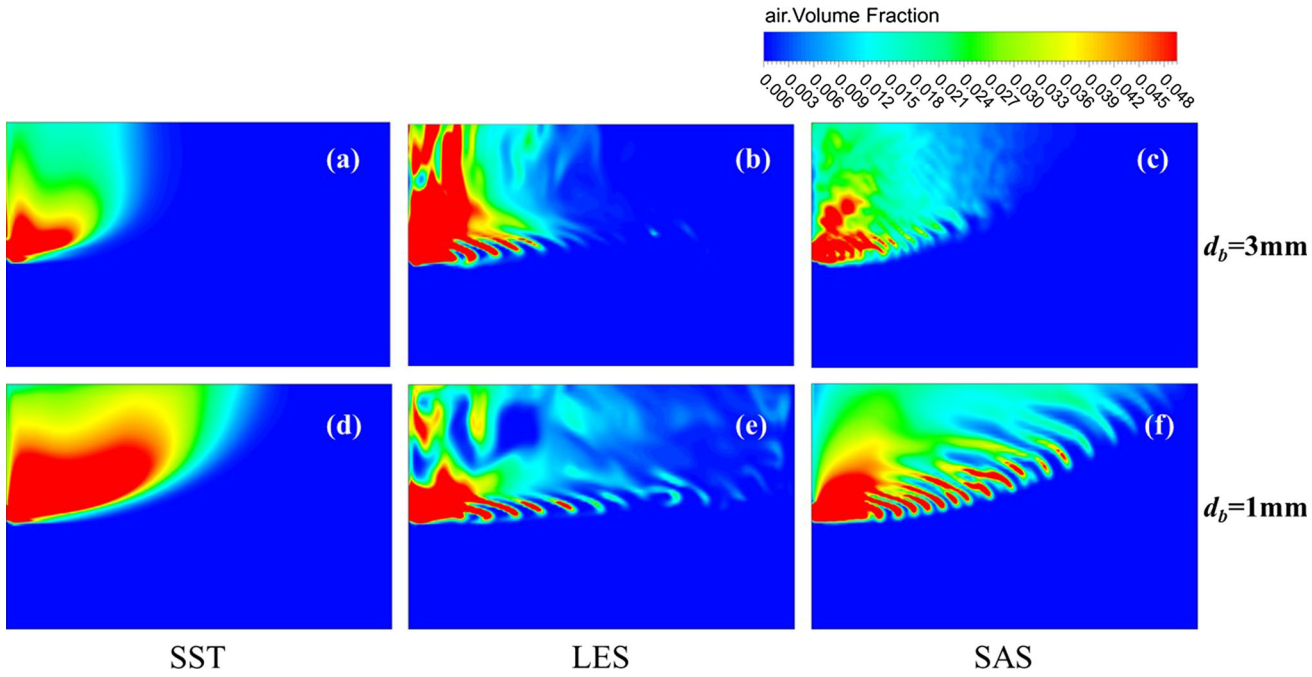

Fig. 2—Predicted air volume fractions in the center plane by different models of SST: (*a*) 3 mm, (*d*) 1 mm; LES: (*b*) 3 mm, (*e*) 1 mm; SAS: (*c*) 3 mm, (*f*) 1 mm (Color figure online).

solution is reached when the residuals of all the variables are less than 10^{-4}. The flow was simulated for the physical time of 100 seconds, and the data of water velocities were monitored during the calculation process. The data were sampled and time-averaged over the last 50 seconds.

IV. RESULTS AND DISCUSSION

A. *Instantaneous Flow Characteristics*

Snapshots of the instantaneous distribution of the gas phase volume fraction are shown in Figure 2 obtained respectively with the SST, LES and SAS turbulence models. They are presented for different bubble diameter of 1 mm and 3 mm and are sampled at the center plane of the simulation domain. The volume fraction field illustrates the dynamics of the formed bubble plume showing a typical fan pattern. For the RANS approach (SST model), the air distribution is more homogenous and steady, as shown in Figures 2(a) and (d). The pulsating motion of the gas phase cannot be captured although the turbulent dispersion force is considered. The reason is that a typical URANS model is applied without taking into account the turbulent length-scale effect. The pulsating motions of air gas can be captured well by LES and SAS methods along the outer front of the jet. The pulsating movement is important to the transport and entrapment of the bubbles and nonmetallic inclusions in the actual casting mold. The corresponding distribution pattern of the gas volume fraction in Figure 2 shows a significant deviation for two bubble diameters. One can see that the smaller bubbles can travel across the mold further than the bigger ones, and their dispersion is broader as well. Concluding, the bubble size is an important factor for the bubble transport and its correct prediction.

In order to visualize the characteristic three-dimensional eddy structure computed by the SAS and LES models, various iso-surfaces of the Q-criterion[43] are given in Figure 3 calculated using following relation:

$$Q = \frac{1}{2}(\Omega^2 - \mathbf{S}^2), \qquad [23]$$

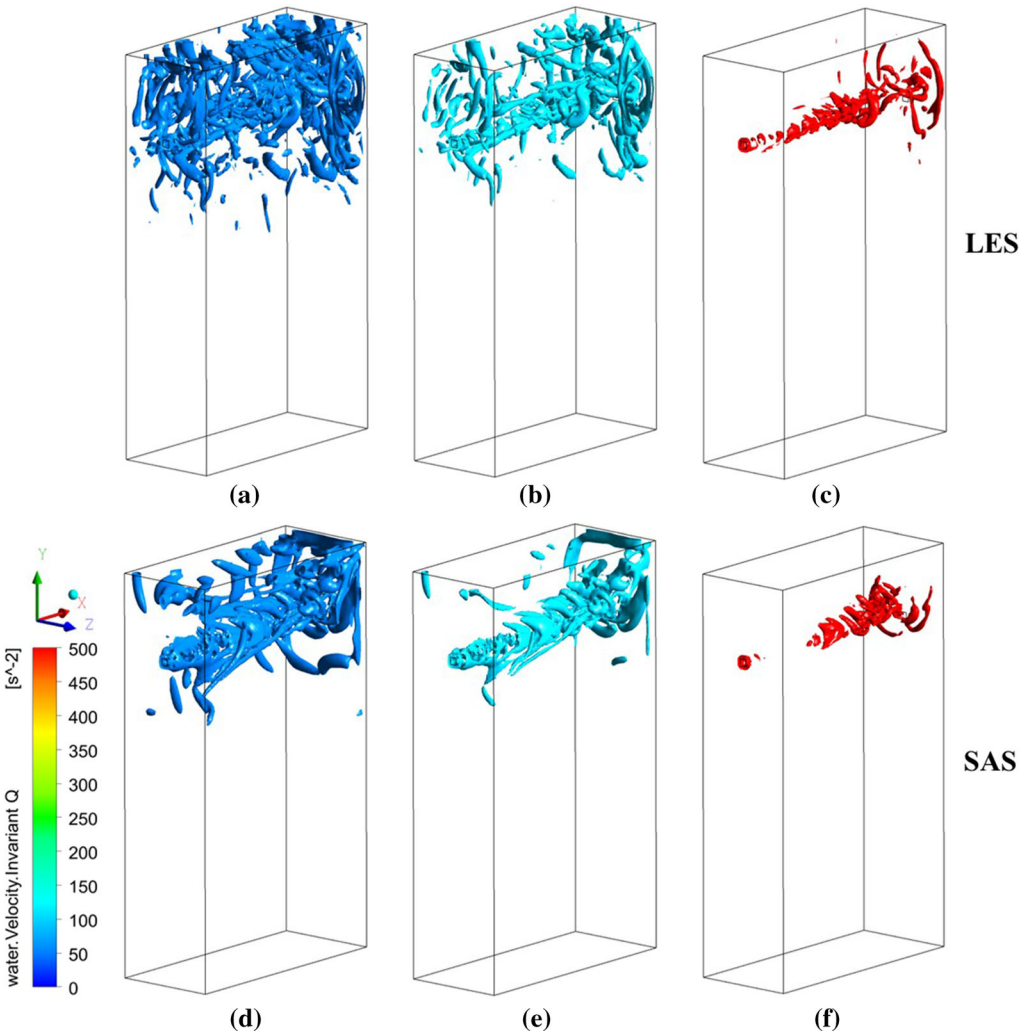

Fig. 3—Instantaneous iso-surfaces of Q-criterion by LES: (*a*) 50 $1/s^2$, (*b*) 100 $1/s^2$, (*c*) 500 $1/s^2$; by SAS: (*d*) 50 $1/s^2$, (*e*) 100 $1/s^2$, and (*f*) 500 $1/s^2$ (Color figure online).

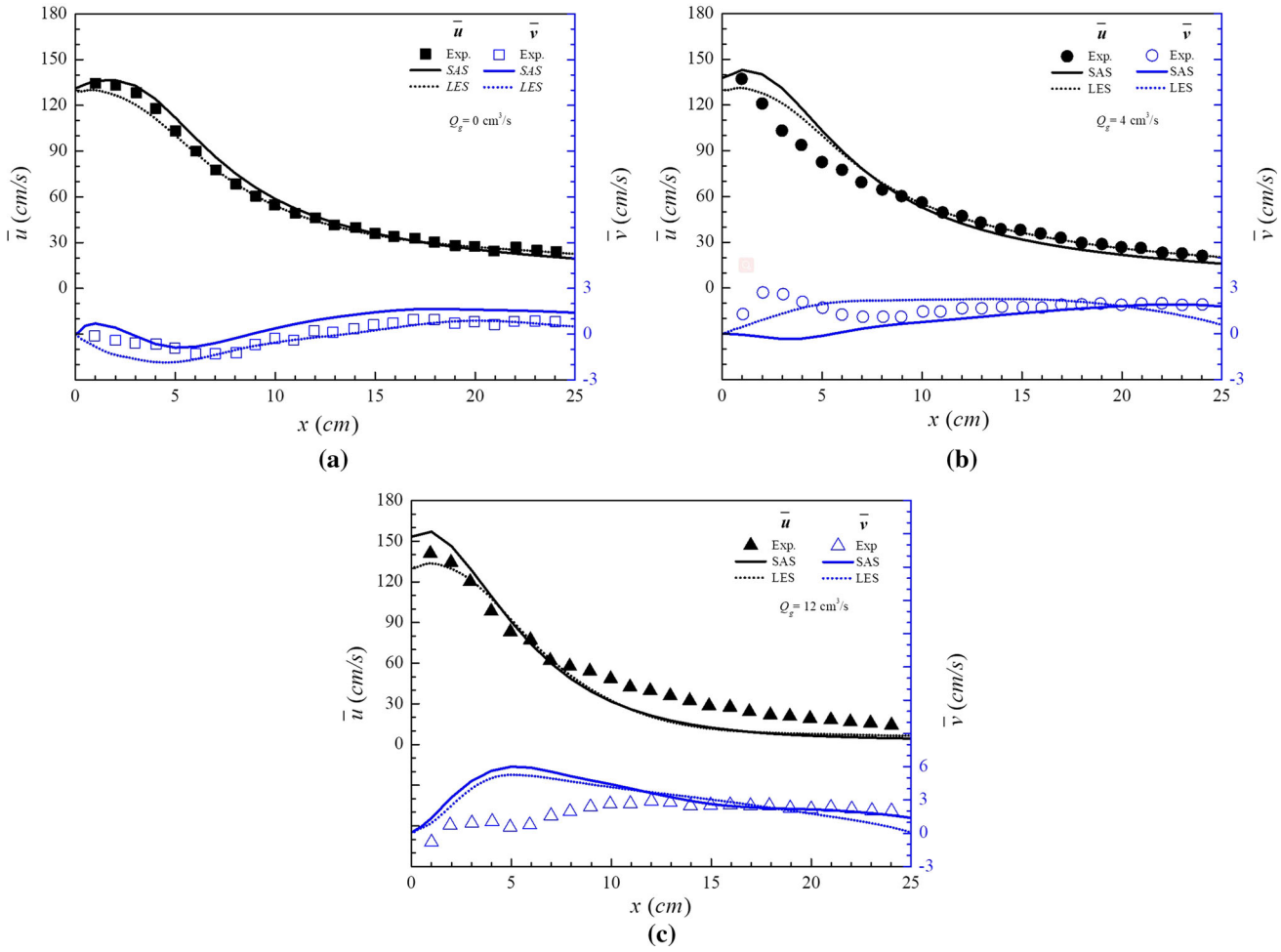

Fig. 4—Comparison between the simulated and experimental profiles for different gas-flow rates (*a*) Q_g = 0 cm^3/s, (*b*) Q_g = 4 cm^3/s, and (*c*) Q_g = 12 cm^3/s (Color figure online).

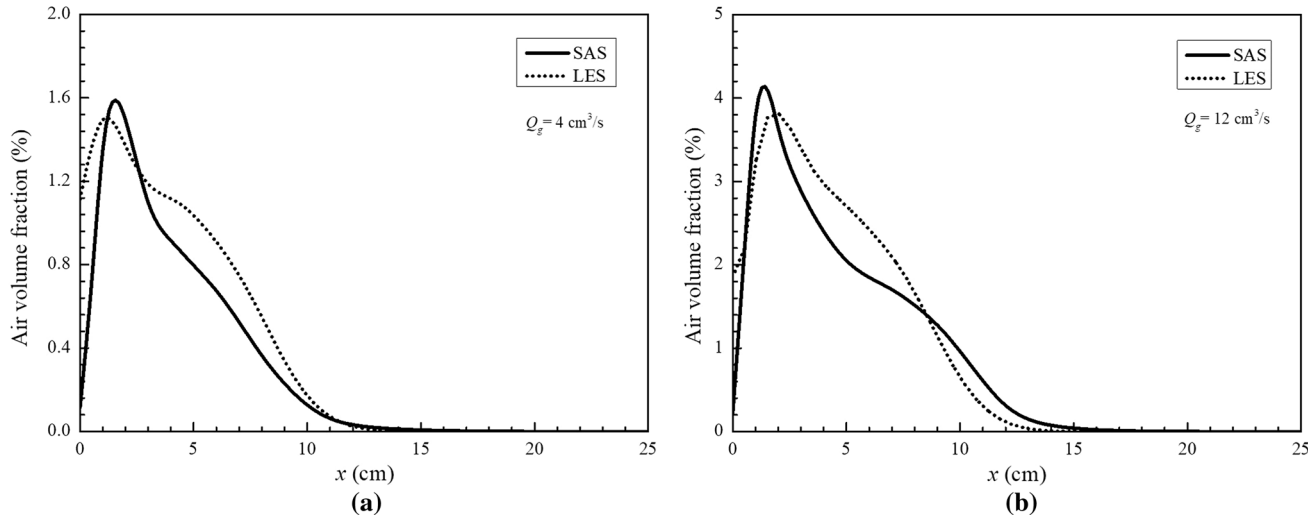

Fig. 5—Predicted averaged air volume fractions for different gas-flow rates (*a*) Q_g = 4 cm^3/s and (*b*) Q_g = 12 cm^3/s.

where Ω is the vorticity tensor.

Both results of the SAS and LES approaches are obtained on the same grid and using the same time step. The strong mixing zone along the liquid jet can be clearly seen from both simulations. Of cause, more sophisticated turbulent structures are captured by the LES model. Compared to conventional URANS model, the SAS model resolves more unsteady structures due to the introduction of the von Karman lengths scale L_{vk}. It is a direct result of the term-by-term modeling of the exact transport equation for the integral length-scale introduced by Rotta as discussed elsewhere.[12] The L_{vk} allows the SAS model to adjust to the already resolved scales in the flow field, thereby avoiding the excessive damping introduced by the conventional URANS.

B. *Time-Averaged Results*

In order to get a quantitative comparison with the experimental data, the time-averaged results are analyzed in this section. The experimental measurements of the time-averaged axial velocity $\bar{u}$ and vertical velocity $\bar{v}$ are taken along the centerline at the nozzle level, as indicated in Figure 1. The applied water flow rate is set to 5 l/min, while the air flow rate is varied from 0 to 12 cm^3/s. The simulation results for both models are averaged for 50 seconds starting from the time instant t = 50 seconds to quantitatively compare with the experimental data.

Figure 4 shows the profiles of the mean axial and vertical velocities for different turbulence models under various gas-flow rates. For the single-phase water jet, shown in Figure 4(a), it can be seen that good quantitative agreement with the experimental data is obtained by both models. The results of SAS simulation have slightly higher values compared with the LES in both profiles. At the low gas-flow rate: Q_g = 4 cm^3/s, as shown in Figure 4(b), both simulations give a better profile prediction for $\bar{u}$ than that for $\bar{v}$. The measured peak value of $\bar{v}$ profile is located at 2 cm away from the nozzle inlet; however, it may be noticed that none of the models could capture it well. The reason most probably is due to the small gas volume fraction predicted by both models, which cannot provide enough lift force for the liquid jet, as shown in Figure 5(a). The predicted time-averaged peak value and the distribution of gas

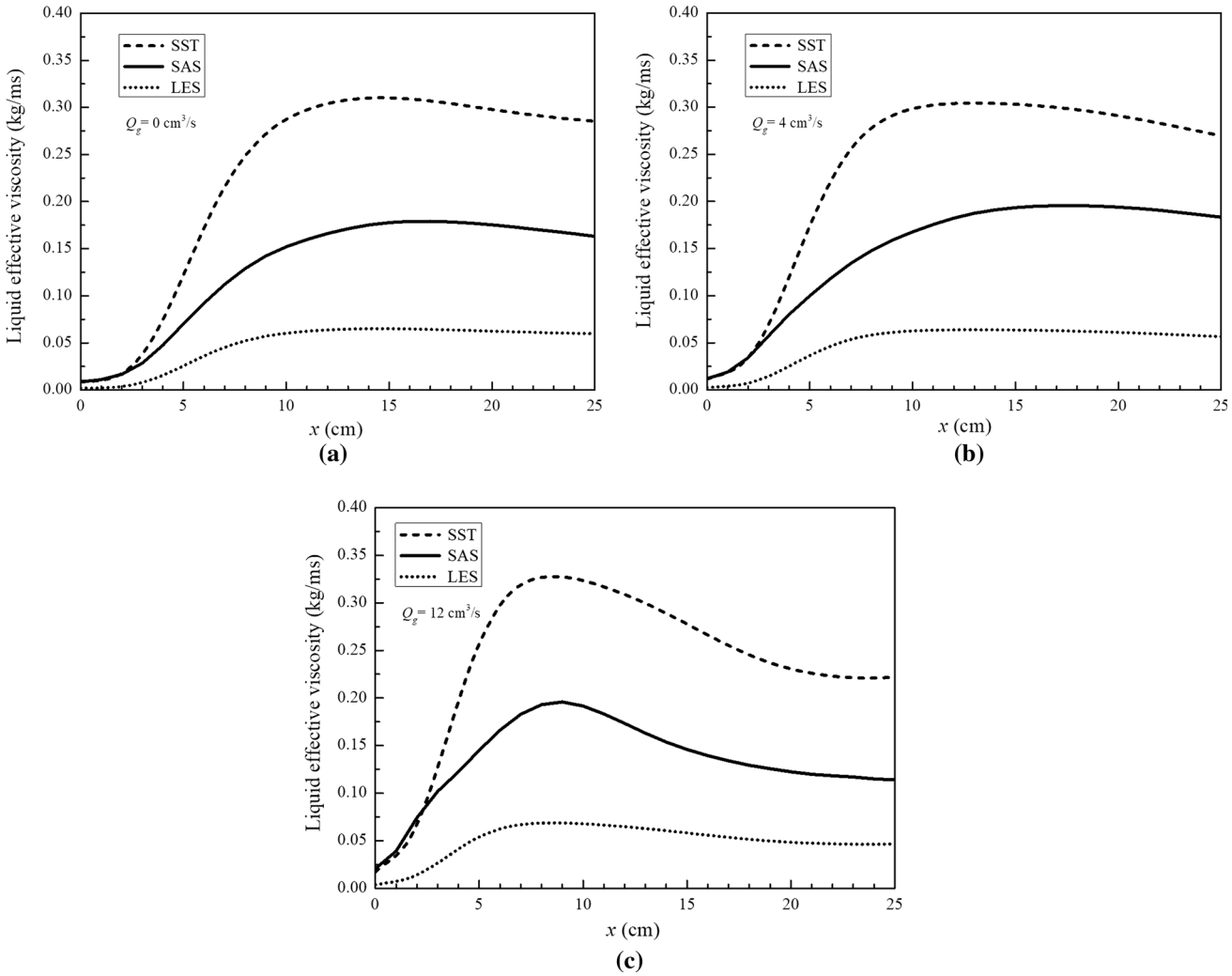

Fig. 6—Predicted averaged liquid's effective viscosities for different gas-flow rates (*a*) Q_g = 0 cm^3/s, (*b*) Q_g = 4 cm^3/s, and (*c*) Q_g = 12 cm^3/s.

volume fraction by SAS model are similar to those obtained with the LES. The prediction of SAS model gives an acceptable result at a distance ranging from 7 to 25 cm away from the nozzle. Figure 4(c) shows the profiles of $\bar{u}$ and $\bar{v}$ for the higher gas-flow rate $Q_g = 12$ cm^3/s. It can be seen that both simulations can predict the experimental trend of $\bar{u}$ profile with acceptable deviation level. For $\bar{v}$ profile, both SAS and LES results overpredict the $\bar{v}$ magnitudes close to the inlet. This effect can be attributed to the predicted higher gas volume fraction near the SEN, as shown in Figure 5(b), at about 4.1 pct, which can lift the jet. It should be especially stressed here that according to the experimental measurements, the peak value of $\bar{v}$ close to the SEN is larger at the lower gas-flow rates. Despite being really confusing, the reliability of the experimental data is respected and accepted here. This effect should be subjected for further study.

Figure 6 presents the comparison of the turbulent effective viscosity predicted respectively by the SST, SAS, and LES turbulence models for different gas-flow rates. It can be seen that the predicted maximum effective viscosity by SST model is about 1.7 times larger than that by SAS; the latter allows avoiding the excessive damping introduced by the conventional URANS approach. However, compared with LES, larger viscosity values were obtained; this variance is attributed to the eddy viscosity computing method seen in Eqs. [13] and [14]. The eddy viscosity ratio Ψ can be defined by

$$\Psi = \frac{\mu_{T,l}^{SAS}}{\mu_{T,l}^{LES}} = \left(\frac{L_{vk}}{C_S C_{SAS} \Delta}\right)^2 \geq \left(\frac{C_{S1} C_{SAS} \Delta}{C_S C_{SAS} \Delta}\right)^2 = \left(\frac{C_{S1}}{C_S}\right)^2 = \left(\frac{2}{C_S}\right)^2 > 1. \quad [24]$$

Therefore, the predicted eddy viscosity by the SAS is larger than that by the LES model. In addition, the liquid's effective viscosity increases with the increasing gas injection rate. Especially at high gas rate of $Q_g = 12$ cm^3/s, a significant peak value is found at about 9 cm away from the nozzle. Unfortunately, a comparison with the experimental data is not possible, since the effective viscosity represents a model variable only and it is hard to relate it with any physical quantity.

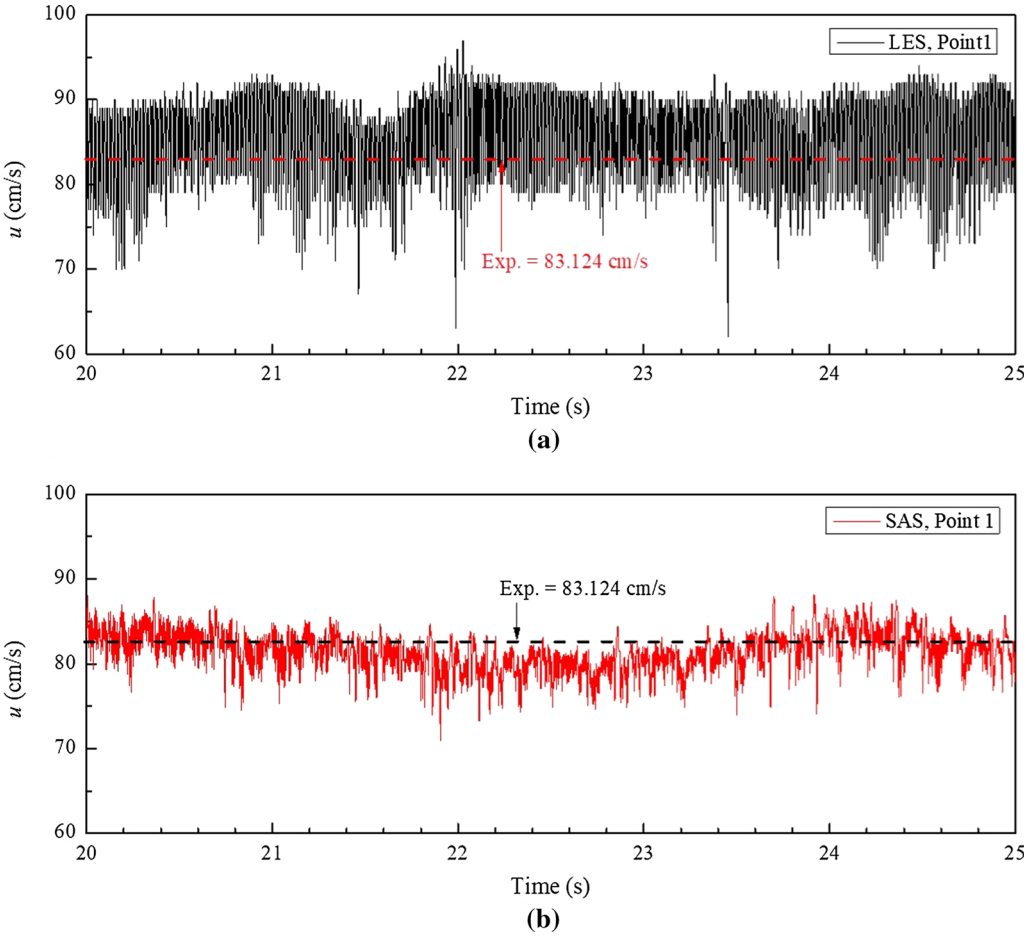

Fig. 7—Time history plots of the axial velocity u at point 1 by (*a*) LES and (*b*) SAS.

C. *Spectral Analysis*

In turbulent flows, a wide range of the length-scales exists, limited by the dimensions of the flow domain and by the diffusive scales of molecular viscosity. Thereby the spectral analysis is a valuable tool to investigate the details of turbulence. Since the SAS model is an improved URANS formulation based on the von Karman turbulent scale, it allows the formation of a turbulent spectrum under the unstable flow conditions. Thereby the power spectrum analysis is performed for both SAS and LES models and presented in this section. Firstly, the transient axial velocity u and vertical velocity v at Point 1 in the jet region (x = 5 mm, y = 0 mm, z = 0 mm) are monitored during the calculating process. Taking the high gas-flow rate (Q_g = 12 cm^3/s) as an example, the transient histories of axial velocity u and vertical velocity v are respectively shown in Figures 7 and 8. The period of 5 seconds presented in these figures corresponds to 5000 sample points for the simulations. It can be seen that both SAS and LES reflect the transient fluctuation behavior, but with different amplitudes of the fluctuations. The stronger amplitude of the fluctuations was found in the LES results. Good agreements with the averaged experimental data for axial velocity u have been observed in both models, but they do not fit well for vertical velocity v, which has been discussed in the Section IV–B.

The transfer of energy is analyzed through the power spectrum densities (PSD) of axial velocity u taken at point 1, as shown in Figures 9 through 11. A fast Fourier transform (FFT) of velocity signal using the Welch method with nonoverlapping sections, and a Hanning window was performed. The frequency domain is resolved from 0.2 to 500 Hz. The lowest frequency is limited by the total data collection time during the simulation of 5 seconds. The highest frequency is half of the signal sampling rate of 1000 Hz. For the single-phase water jet, as shown in Figure 9, it is seen that the PSD is very similar between two cases; the results of LES show higher values compared with the SAS. The classical − 5/3 law is maintained properly for both turbulent models according to the single-phase turbulent-flow calculations proposed by Van Cauwenberge *et al.*[44] When the air gas is injected, as shown in Figures 10 and 11, the predictions for the SAS model are in good agreement with the LES in the low-frequency region. Hence, the large-scale eddies' magnitudes can be well captured by the current SAS model. The classical − 5/3 PSD slope is violated,[45] since the decay

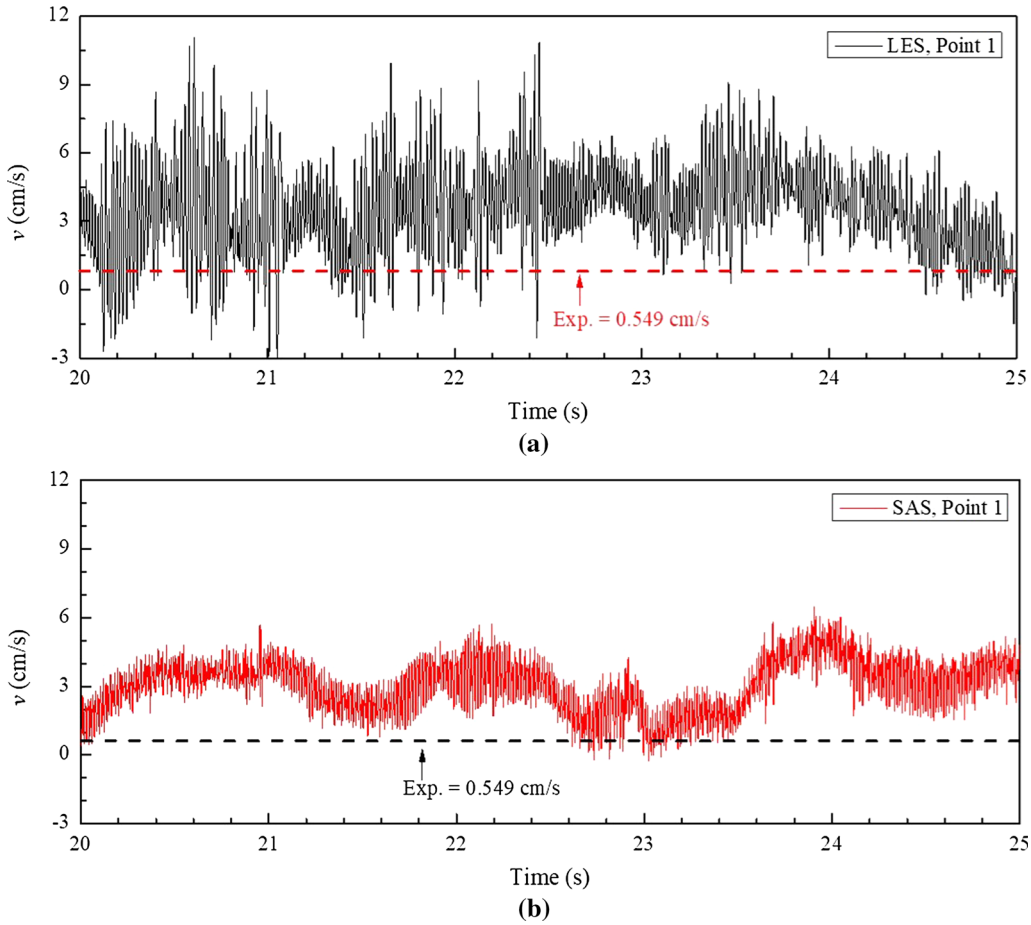

Fig. 8—Time history plots of the vertical velocity v at point 1 by (*a*) LES and (*b*) SAS.

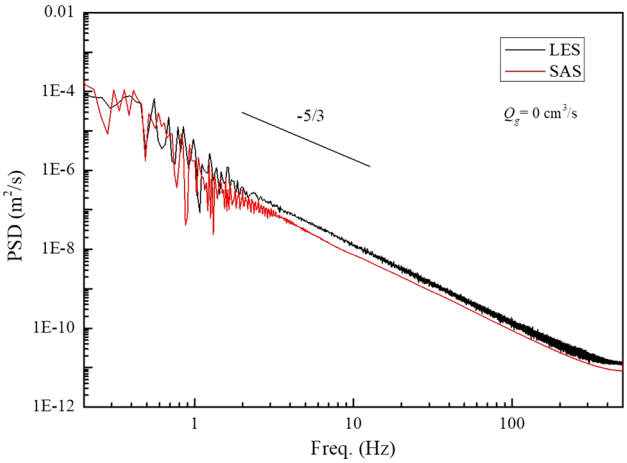

Fig. 9—Power spectrum densities of axial velocity u at point 1 under $Q_g = 0$ cm^3/s (Color figure online).

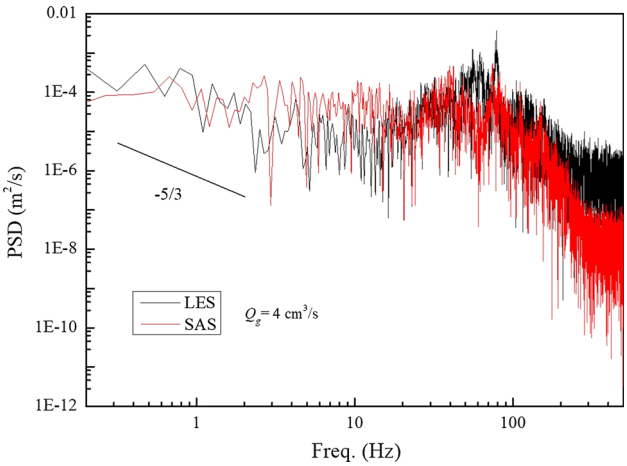

Fig. 10—Power spectrum densities of axial velocity u at point 1 under $Q_g = 4$ cm^3/s (Color figure online).

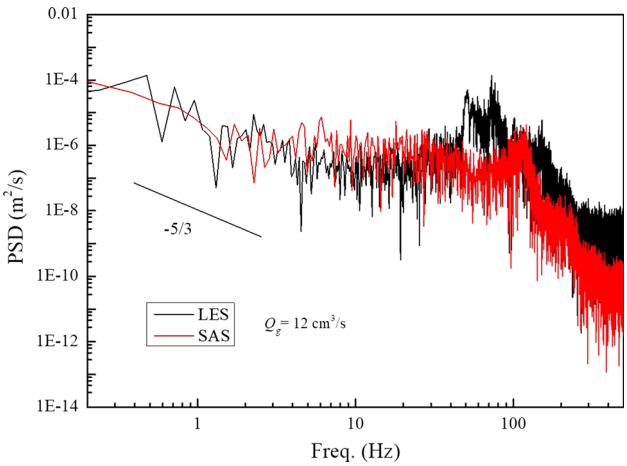

Fig. 11—Power spectrum densities of axial velocity u at point 1 under $Q_g = 12$ cm^3/s (Color figure online).

is too strong for the high frequencies above 70 Hz. Due to the larger eddy viscosity, the PSD of SAS is more damped at the high-frequency spectrum.

V. CONCLUSIONS

The primary goal of this study was to assess the application of the SAS turbulence model in modeling the transient two-phase flow in the continuous-casting process. The predicted results by the SAS model show good agreement with the results of the experiment and the LES model, both for the time-averaged velocity field and the transient-flow characteristics. The conclusions are summarized as follows:

The introduction of the von Karman length-scale into the turbulence-scale equation allows the SAS model to dynamically adjust to the resolved turbulent structures, avoiding the excessive damping introduced by the conventional URANS models. The LES-like pulsating behavior and large-scale eddy magnitudes at the unsteady regimes of the multiphase turbulent flow are captured.

The SAS model shows a wide turbulent spectrum. The classical − 5/3 law of power spectrum densities (PSD) of axial velocity is obeyed properly for the single-phase flow. For the two-phase flow, the predictions are in a good agreement with the LES in the low-frequency region. The classical − 5/3 PSD slope is violated for the multiphase flow, while strong decay for the frequencies > 70 Hz is detected. The PSD is underestimated by SAS model at high frequencies.

In conclusion, the SAS model offers an attractive alternative to the existing LES approach or to the other hybrid RANS/LES models for the strong unsteady flows. It can be a promising option worthy of adoption in conjunction with the Euler–Euler model to predict the bubbly flow.

ACKNOWLEDGMENTS

This work was financially supported by the Fundamental Research Funds for the Central Universities of China (No. N162504009), the National Natural Science Foundation of China (Nos. 51604070 and 51574068) and the China Scholarship Council (No. 201706085027). The financial supports by the RHI-Magnesita AG; the Austrian Federal Ministry of Economy, Family, and Youth; and the National Foundation for Research, Technology, and Development within the framework of the Christian Doppler Laboratory for Advanced Process Simulation of Solidification and Melting are gratefully acknowledged.

REFERENCES

1. M. Iguchi and N. Kasai: *Metall. Mater. Trans. B*, 2000, vol. 31B, pp. 453–60.

2. B.G. Thomas, L.J. Mika, and F.M. Najjar: *Metall. Mater. Trans. B*, 1990, vol. 21B, pp. 387–400.
3. L. Zhang, S. Yang, K. Cai, J. Li, X. Wan, and B.G. Thomas: *Metall. Mater. Trans. B*, 2007, vol. 38B, pp. 63–83.
4. A.N. Kolmogorov: *Dokl. Akad. Nauk SSSR*, 1941, vol. 32, pp. 16–18.
5. A. Issakhov: *J. Comput. Commun.*, 2013, vol. 1, pp. 1–5.
6. S.B. Pope: *Turbulent Flows*, Cambridge University Press, Cambridge, 2000, pp. 346–50.
7. Y. Miki and S. Takeuchi: *ISIJ Int.*, 2003, vol. 43, pp. 1548–55.
8. Q. Yuan, S. Sivaramkrishnan, S.P. Vanka, and B.G. Thomas: *Metall. Mater. Trans. B*, 2004, vol. 35B, pp. 967–82.
9. A. Ramos-Banderas, R. Sánchez-Perez, R.D. Morales, J. Palafox-ramos, L. Demedices-Garcia, and M. Diaz-cruz: *Metall. Mater. Trans. B*, 2004, vol. 35B, pp. 449–60.
10. C. Real, R. Miranda, C. Vilchis, M. Barron, L. Hoyos, and J. Gonzalez: *ISIJ Int.*, 2006, vol. 46, pp. 1183–91.
11. Z.Q. Liu, B.K. Li, and M.F. Jiang: *Metall. Mater. Trans. B*, 2014, vol. 45B, pp. 675–97.
12. F.R. Menter: *Int. J. Comput. Fluid*, 2009, vol. 23, pp. 305–16.
13. F.R. Menter and Y. Egorov: *Flow Turbul. Combust.*, 2010, vol. 85, pp. 113–38.
14. Y. Egorov, F.R. Menter, R. Lechner, and D. Cokljat: *Flow Turbul. Combust.*, 2010, vol. 85, pp. 139–65.
15. B.G. Thomas, X. Huang, and R.C. Suaaman: *Metall. Mater. Trans. B*, 1994, vol. 25B, p. 527.
16. D. Creech: Master's thesis, University of Illinois at Urbana Champaign, Urbana, IL, 1999.
17. H. Bai and B.G. Thomas: *Metall. Mater. Trans. B*, 2001, vol. 32B, pp. 253–67.
18. A. Ramos-Banderas, R.D. Morales, R. Sanchez-Perez, L. Garcia-Demedices, and G. Solorio-Diaz: *Int. J. Multiphase Flow*, 2005, vol. 31, pp. 643–65.
19. J. Klostermann, H. Chaves, and R. Schwarze: *Steel Res. Int.*, 2007, vol. 78, pp. 595–601.
20. J.O. Hinze: *Turbulence*, McGraw-Hill, New York, 1975.
21. Z.Q. Liu, B.K. Li, M.F. Jiang, and F. Tsukihashi: *ISIJ Int.*, 2014, vol. 54, pp. 1314–23.
22. Q. Yuan, T. Shi, S.P. Vanka, and B.G. Thomas: *Computational Modeling of Materials*, Minerals and Metals Processing, Warrendale, PA, 2001, pp. 491–500.
23. Z.Q. Liu, F.S. Qi, B.K. Li, and S.C.P. Cheung: *Int. J. Multiphase Flow*, 2016, vol. 79, pp. 190–201.
24. Z.Q. Liu, F.S. Qi, B.K. Li, and M.F. Jiang: *Metall. Mater. Trans. B*, 2015, vol. 46B, pp. 933–52.
25. Z.Q. Liu, B.K. Li, F.S. Qi, and S.C.P. Cheung: *Powder Technol.*, 2017, vol. 319, pp. 139–47.
26. K. Timmel, C. Kratzsch, A. Asad, D. Schurmann, R. Schwarze, and S. Eckert: *IOP Conference Series: Materials Science and Engineering*, 2017, vol. 228, p. 012019. https://doi.org/10.1088/1757-899x/228/1/012019.
27. S. Sarkar, V. Singh, S.K. Ajmani, R.K. Singh, and E.Z. Chacko: *ISIJ Int.*, 2018, vol. 58, pp. 68–77.
28. Z.Q. Liu, B.K. Li, M.F. Jiang, and F. Tsukihashi: *ISIJ Int.*, 2013, vol. 53, pp. 484–92.
29. Z.Q. Liu and B.K. Li: *Metall. Mater. Trans. B*, 2017, vol. 48B, pp. 1833–49.
30. B.G. Thomas: *Steel Res. Int.*, 2018, vol. 89, p. 1700312.
31. J. Frohlich and D. von Terzi: *Prog. Aerosp. Sci.*, 2008, vol. 44, pp. 349–77.
32. T. Ma, D. Lucas, T. Ziegenhein, J. Frohlich, and N.G. Deen: *Chem. Eng. Sci.*, 2015, vol. 131, pp. 101–08.
33. C. Kratzsch, A. Asad, and R. Schwarze: *J. Manuf. Sci. Prod.*, 2015, vol. 15, pp. 49–57.
34. H.A. Jakobsen, B.H. Sannaes, S. Grevskott, and H.F. Svendsen: *Ind. Eng. Chem. Res.*, 1997, vol. 36, pp. 4052–74.
35. M.T. Dhotre, B. Niceno, and B.L. Smith: *Chem. Eng. J.*, 2008, vol. 136, pp. 337–48.
36. Y. Sato, M. Sadatomi, and K. Sekiguchi: *Int. J. Multiphase Flow*, 1975, vol. 2, pp. 79–87.
37. F.R. Menter: AIAA Paper #93-2906, *24th Fluid Dynamics Conference*, July 1993.
38. J. Smagorinsky: *Month. Weather Rev.*, 1963, vol. 91, pp. 99–165.
39. M. Germano, U. Piomelli, P. Moin, and W.H. Cabot: *Phys. Fluids A*, 1991, vol. 3, pp. 1760–65.
40. D.K. Lilly: *Phys. Fluids A*, 1992, vol. 4, pp. 633–35.
41. M. Ishii and N. Zuber: *AIChE J.*, 1979, vol. 25, pp. 843–55.
42. D.A. Drew and R.T. Lahey: *Int. J. Multiphase Flow*, 1987, vol. 13, pp. 113–21.
43. J.C.R. Hunt, A.A. Wray, and P. Moin: *Center for Turbulence Research Report*, 1988, pp. 193–208.
44. D.J. Van Cauwenberge, C.M. Schietekat, J. Floré, K.M. Van Geem, and G.B. Marin: *Chem. Eng. J.*, 2015, vol. 282, pp. 66–76.
45. Z.Q. Liu and B.K. Li: *Chem. Eng. J.*, 2018, vol. 338, pp. 465–77.